



Photo-assisted synthesis of Ag_3PO_4 /reduced graphene oxide/Ag heterostructure photocatalyst with enhanced photocatalytic activity and stability under visible light



Can Cui ^{a,*}, Yaping Wang ^a, Dayu Liang ^a, Wei Cui ^b, Haihua Hu ^c, Bingqing Lu ^a, Sheng Xu ^a, Xiaoyun Li ^a, Chong Wang ^b, Yu Yang ^b

^a Center for Optoelectronics Materials and Devices, Department of Physics, Zhejiang Sci-Tech University, Hangzhou 310018, China

^b Institute of optoelectronic Information Materials, Yunnan University, Kunming 650091, China

^c Zhejiang University City College, Hangzhou 310015, China

ARTICLE INFO

Article history:

Received 5 December 2013

Received in revised form 19 March 2014

Accepted 6 April 2014

Available online 13 April 2014

Keywords:

Ag_3PO_4

Reduced graphene oxide

Ag nanocrystals

Visible-light-driven photocatalyst

ABSTRACT

A novel Ag_3PO_4 /reduced graphene oxide/Ag nanocrystals ($\text{Ag}_3\text{PO}_4/\text{RGO}/\text{Ag}$) heterostructure photocatalyst has been synthesized using a facile photo-assisted reduction method for the first time. The $\text{Ag}_3\text{PO}_4/\text{RGO}/\text{Ag}$ that consists of close chemical bonding between RGO and Ag_3PO_4 nanoparticles as well as dispersive plasmonic Ag nanocrystals on the RGO sheets exhibited superior photocatalytic activity and stability to bare Ag_3PO_4 , $\text{Ag}/\text{Ag}_3\text{PO}_4$ and $\text{Ag}_3\text{PO}_4/\text{GO}$ in degradation of Rhodamine B and phenol under visible light. It is suggested that the photo-generated electrons in Ag_3PO_4 can be transferred to RGO/Ag, leading to efficient separation and transfer of electron–hole pairs. Meanwhile, under light irradiation, the plasmonic Ag nanocrystals also generate electron–hole pairs through surface plasmon resonance (SPR), in which the active electrons can facilitate the formation of additional active species of $\text{O}_2\bullet^-$ for photocatalysis whereas the holes can be filled by electrons from RGO. As a result, both the photocorrosion of Ag_3PO_4 and the recombination of electron–hole pairs are suppressed due to the special electron transfer route of $\text{Ag}_3\text{PO}_4 \rightarrow \text{RGO} \rightarrow \text{Ag}$ in the heterostructure. This work suggests that the reasonable combination of semiconductors and graphene decorated with noble metallic nanocrystals can provide a versatile strategy for the synthesis of high efficient heterostructured photocatalysts.

© 2014 Elsevier B.V. All rights reserved.

1. Introduction

Photocatalysts, especially those with high photocatalytic activity and strong stability under visible light, have been regarded as promising materials for application in solar energy conversion and water pollutant treatment [1,2]. Up to now, numerous visible-light-driven photocatalysts, such as Ag-based photocatalysts [3–5], doped TiO_2 [6], Bi_2WO_6 [7], CaBi_2O_4 [8] have been developed for photocatalytic water-splitting and photocatalytic degradation of organics in wastewater or air. The silver orthophosphate (Ag_3PO_4) with high photocatalytic performance discovered by Ye and co-workers is regarded as a significant breakthrough in the field of visible-light-driven photocatalysts [9]. This novel photocatalyst exhibits excellent photo-oxidative capabilities for O_2 evolution from water splitting as well as highly efficient organic molecule decomposition activity under visible light [10–12]. However, the

practical application of Ag_3PO_4 is limited by some drawbacks, including the seriously photocorrosion in photocatalysis process, the high cost of using Ag-containing chemicals as starting material, and the poor dispersivity in aqueous solution. The photocorrosion of Ag_3PO_4 has been studied intensively and the basic principles have been well established [13]. Generally speaking, without any sacrificial electron acceptors in aqueous solution, the photo-generated electrons in Ag_3PO_4 can reduce lattice Ag^+ into metallic Ag, which results in the serious decrease of photocatalytic activity of Ag_3PO_4 . Addressing the photocorrosion of Ag_3PO_4 , Ag_3PO_4 -based heterostructured photocatalysts, such as AgX ($\text{X} = \text{Cl}, \text{Br}, \text{I}$)/ Ag_3PO_4 [14], $\text{TiO}_2/\text{Ag}_3\text{PO}_4$ [15], carbon quantum dots/ Ag_3PO_4 [16] have been developed to improve the stability and activity of Ag_3PO_4 due to the fast electron separation and transfer in these heterostructures.

Very recently, the reports of $\text{Ag}_3\text{PO}_4/\text{GO}$ provide an opportunity for the large-scale preparation of highly active visible-light-driven photocatalysts with good stability [17–22]. These studies confirmed that GO in $\text{Ag}_3\text{PO}_4/\text{GO}$ heterostructure can act as an electron acceptor to suppress the charge recombination and

* Corresponding author. Tel.: +86 0571 86843832.

E-mail addresses: cancui@zstu.edu.cn, msecuican@hotmail.com (C. Cui).

prevent the photocorrosion of Ag_3PO_4 . However, GO is a modified graphene with numerous of hydroxyl, carbonyl, carboxylic groups and lots of structure defects on the surface, which lead to its poor electronic conductivity and make it far from requires for working as function materials in photocatalysts or other photoelectrochemical devices. Instead, the RGO sheets obtained from partial reduction of GO in solution have better electronic conductivity than GO and is a suitable substitute of GO for facilitating efficient charge separation and transfer in the heterostructure photocatalysts. Therefore, the effective reduction of GO into RGO is always involved in the preparation of graphene-based photocatalysts. The traditional reduction methods including the chemical reduction [23], thermal reduction [24], and electrochemical reduction [25] have the intrinsic drawbacks, such as involvement of toxic chemicals like hydrazine, requiring rapid heating processes and the need for special instruments, which limit their practical applications. Photoreduction of GO is an effective and green method to produce RGO with the photoexcited semiconductor photocatalysts [26,27], however, the underlying mechanisms of the photo-assisted synthesis of Ag_3PO_4 /RGO composite from Ag_3PO_4 /GO precursor and the photocatalytic performance of Ag_3PO_4 /RGO composite are not well understood [28].

Another interesting issue is the inevitable appearance of metallic Ag nanoparticles on the surface of Ag_3PO_4 under light irradiation [29,30], which is a double edged sword in the photocatalytic performance. The excess Ag nanoparticles on the surface of Ag_3PO_4 would inevitably cover active sites and prevent visible light absorption [29,31], and hence cause a dramatically decrease of photocatalytic activity, while a small load of Ag nanocrystals in the hybrid could improve the electron transfer and visible light absorption due to the SPR effect [30,32]. Therefore, the load and position of the plasmonic Ag nanocrystals in the semiconductor photocatalyst is primary important for the final photocatalytic performance. Considering the synergistic effect of RGO and Ag nanocrystals on the photocatalytic performance, a novel Ag_3PO_4 /RGO/Ag heterostructured photocatalyst, in which most of the plasmonic Ag nanocrystals are selectively grown on RGO sheets rather than on the surface of Ag_3PO_4 particles, is proposed to have better photocatalytic activity and stability than the former reported Ag_3PO_4 /GO or Ag_3PO_4 /RGO nanocomposites [28,33].

In this paper, Ag_3PO_4 /RGO/Ag heterostructure photocatalyst, which consists of Ag_3PO_4 /RGO with close interfacial contact and well dispersive plasmonic Ag nanocrystals on RGO sheets, has been developed using a facile photo-assisted reduction method. The as-prepared Ag_3PO_4 /RGO/Ag exhibited high photocatalytic activity and good stability in degradation of Rhodamine B (RhB) and phenol in aqueous solution under visible light. The mechanism for the synthesis, the enhanced photocatalytic activity and stability of Ag_3PO_4 /RGO/Ag has been thoroughly investigated.

2. Experimental

2.1. Materials

All the chemicals were of analytical grade and used without further purification. Natural graphite and RhB were purchased from Fisher scientific (Hong Kong) Ltd. Co. Sodium nitrate (NaNO_3), potassium permanganate (KMnO_4), hydrogen peroxide (H_2O_2), concentrated sulfuric acid (H_2SO_4), hydrochloric acid (HCl), hydrazine, silver nitrate (AgNO_3), disodium dihydrogen phosphate hydrate ($\text{Na}_2\text{HPO}_4 \cdot 12\text{H}_2\text{O}$), phenol and methanol were purchased from Sigma-Aldrich. The deionized water was produced from a Millipore Milli-Q water purification system and used throughout the whole experiments.

2.2. Synthesis of Ag_3PO_4 and Ag_3PO_4 /GO

GO suspension was synthesized through chemical exfoliation of graphite powder via a modified Hummers' method [34]. A RGO sample was prepared from the reduction of GO with hydrazine for comparison [35]. Ag_3PO_4 /GO was synthesized by a simple precipitation method [17–22]. In a typical preparation process, 0.5096 g of AgNO_3 was dissolved in 50 mL of 0.5 mg/mL GO aqueous solution to obtain a homogeneous suspension. After ultrasonic treatment for 30 min, the electrostatically driven assembly of positively charged Ag^+ on the negatively charged GO sheets was achieved. Then 50 mL of 0.015 M Na_2HPO_4 aqueous solution was added drop by drop into the above suspension with vigorous magnetic stirring in dark condition at room temperature. It should be mentioned that the Ag^+ was excess in our synthesis process and there were a lots of residual Ag^+ that remain on the GO sheets after the formation of Ag_3PO_4 /GO nanocomposite. The brown precipitate of Ag_3PO_4 /GO was collected by centrifugation at 6000 rpm for 10 min and then rinsed repeatedly with deionized water and absolute ethanol for several times. Finally, the precipitate was dried in a vacuum oven at 60 °C for 2 h. The yellow Ag_3PO_4 powder sample was prepared under the same condition without adding of GO.

2.3. Synthesis of heterostructured $\text{Ag}/\text{Ag}_3\text{PO}_4$ and Ag_3PO_4 /RGO/Ag

Ag_3PO_4 /RGO/Ag was prepared by a photo-assisted reduction treatment from unrinse Ag_3PO_4 /GO precursor. Briefly, 0.3 g of Ag_3PO_4 /GO was well dissolved in 100 mL absolute ethanol and then exposed to visible-light irradiation for 30 min (250 W tungsten halogen lamp with an ultraviolet cutoff filter that provides visible light $\lambda \geq 400$ nm). The grey precipitate of Ag_3PO_4 /RGO/Ag was collected by centrifugation at 6000 rpm for 10 min and then rinsed repeatedly with deionized water and absolute ethanol for several times. The powder sample was finally dried in a vacuum oven at 60 °C for 2 h. The dark $\text{Ag}/\text{Ag}_3\text{PO}_4$ sample was prepared under the same condition by replacing the Ag_3PO_4 /GO precursor with Ag_3PO_4 .

2.4. Characterizations

The phase structure of the samples was characterized by X-ray diffraction (XRD) on a Bruker D8 diffractometer using $\text{Cu K}\alpha$ ($\lambda = 1.5406 \text{ \AA}$) radiation at 40 kV and 40 mA. Scanning electron microscopy (SEM) images were taken on a Hitachi S-4800 field emission scanning electron microscope at a voltage of 20 kV. Transmission electron microscopy (TEM) images were conducted using a JEM-2100 microscope at an accelerating voltage of 200 kV. Fourier transform infrared (FTIR) spectra were recorded on a Nicolet Avatar 370 spectrometer with powder samples embedded in KBr disks. Raman spectra were measured by a triple-stage laser Raman spectrum system (Horiba JY-T64000, France) with a 514 nm laser. The X-ray photoelectron spectroscopy (XPS) were performed using a Kratos Axis Ultra system (Kratos Analytical Ltd., Manchester, UK) with monochromatic Al $\text{K}\alpha$ X-rays (1486.6 eV) operated at 10 mA and 15 kV, and with a background pressure of approximately 5.0×10^{-9} Torr. The resulting binding energies were calibrated to the C1s (284.6 eV) peak. The UV-vis diffuse reflectance spectra (UVDRS) were obtained on a Perkin Elmer Lambda 900 UV-vis spectrophotometer by using BaSO_4 as the matrix. The photoluminescence (PL) spectra were obtained on a Hitachi F7000 at an excitation wavelength of 300 nm.

2.5. Photocatalytic activity measurement

The photocatalytic performance tests were carried out by degradation of RhB and phenol under atmospheric pressure in

a quartz reactor system. In a typical process, 50 mg of photocatalyst was added into 50 mL RhB or phenol aqueous solution (20 ppm). The suspension was stirred in dark for 30 min to establish an adsorption-desorption equilibrium. Then the suspension was exposed to a 250 W tungsten halogen lamp with an ultraviolet cutoff filter (providing visible light $\lambda \geq 400$ nm) under magnetic stirring. During illumination, a circulation of water through an external cooling coil was conducted to maintain the temperature of suspension at about 25 °C. At 5 min interval of visible-light irradiation, 3 mL of the suspension was collected and centrifuged at 4000 rpm for 10 min to remove photocatalyst particles for analysis. Variations in the concentration of RhB or phenol were monitored using an UNICO UV-4802H UV-vis spectrophotometer and an Agilent Technologies 1260 high performance liquid chromatography (HPLC) that equipped with an UV-vis detector and an Eclipse XDB-C18 reversed phase column (3.5 μ m, 4.6 mm \times 150 mm). The mobile phase using in HPLC analysis was water/methanol (50:50, v/v) with a flow rate of 0.5 mL/min.

2.6. Detection of reactive oxidative species

The reactive oxidative species in the photodegradation were detected with in-situ trapping experiments. The detection process is similar to the photodegradation experimental process. Three different scavengers, *p*-benzoquinone (BQ, $O_2\bullet^-$ radicals scavenger), disodium ethylenediaminetetraacetate (EDTA, holes scavenger) and isopropanol (IPA, $OH\bullet$ radicals scavenger) were added into the RhB solution prior to the addition of the photocatalyst in three different photodegradation experiments and the concentration of scavengers was set at 1.0 mM.

2.7. Photoelectrochemical measurements

The transient photocurrent characterization were measured using a CHI660D electrochemical analysis instrument and operated in a standard three-compartment cell, consisting of a working electrode, a platinum counter electrode, and an Ag/AgCl reference electrode. The electrolyte was 0.1 M Na_2SO_4 aqueous solution degassed with N_2 and the illumination source was a 150 W halogen tungsten lamp with an ultraviolet cutoff filter that provides visible light ($\lambda > 400$ nm). The working electrodes were prepared by the doctor-blade method on fluorine-doped SnO_2 (FTO) conductive glass. Briefly, 0.1 g of photocatalyst and 200 μ L of 0.5 mg/mL nafion solution were dissolved in 1.0 mL of absolute ethanol to form a homogeneous suspension and then dried at 60 °C for 2 h to form slurry. The slurry was coated onto FTO glass to form a uniform film, and then heated in vacuum at 200 °C for 2 h.

3. Results and discussion

3.1. Characterization of photocatalysts

Fig. 1 shows the XRD patterns of GO, RGO, Ag_3PO_4 , Ag/Ag_3PO_4 , Ag_3PO_4/GO and $Ag_3PO_4/RGO/Ag$. The XRD pattern of GO reveals a characteristic reflection peak at $2\theta = 10.6^\circ$, corresponding to a *d*-spacing of 0.83 nm in the lamellar structure of GO [36]. In the XRD pattern of RGO, the characteristic peak of GO at $2\theta = 10.6^\circ$ is disappeared and replaced by a weak broad peak at $2\theta = 25^\circ$ (corresponding to a *d*-spacing of 0.36 nm) [35,36]. As for the pattern of Ag_3PO_4 , all the diffraction peaks can be indexed to the body-centered cubic phase of Ag_3PO_4 (JCPDS card No. 06-0505). The Ag_3PO_4/GO exhibits a similar XRD pattern as pure Ag_3PO_4 , suggesting that the incorporation of GO sheets has little influence on the crystallite size and phase structure of Ag_3PO_4 . The diffraction peaks at 37.7° in the patterns of Ag/Ag_3PO_4 and $Ag_3PO_4/RGO/Ag$ match well with the (111) planes of the face-centered cubic structure

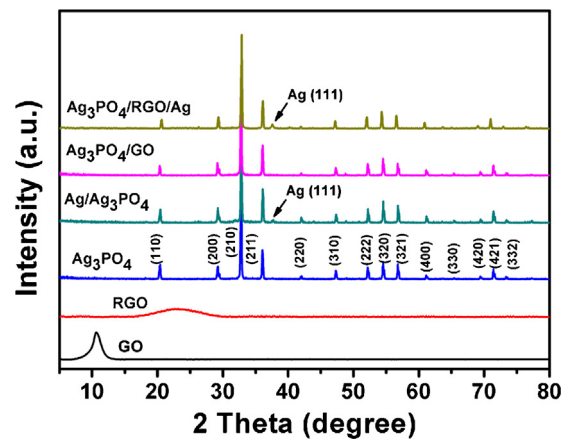


Fig. 1. XRD patterns of GO, RGO, Ag_3PO_4 , Ag/Ag_3PO_4 , Ag_3PO_4/GO , and $Ag_3PO_4/RGO/Ag$.

Ag (JCPDS card No. 04-0783), indicating the formation of metallic Ag in these nanocomposites. However, the characteristic diffraction peak of GO at 10.6° and the peak of RGO at 25° are absent in the XRD patterns of Ag_3PO_4/GO and $Ag_3PO_4/RGO/Ag$, which may be attributed to relatively low diffraction intensity and the destruction of the regular stacking of graphene sheets by the incorporation of Ag_3PO_4 nanoparticles [37]. The average crystallite size of Ag_3PO_4 nanoparticles in the pure phase and the composites are estimated to be around 50 nm with the Scherrer equation based on the three diffraction peaks of (210) at 33.3°, (211) at 36.6° and (320) at 55.0°.

The photoreduction of GO into RGO with the assistance of Ag_3PO_4 under visible-light irradiation was investigated with the FTIR, Raman and XPS spectra. Fig. 2(a) shows the FTIR spectra of the photocatalysts. The characteristic peaks at 1720, 1630 and 1058 cm^{-1} in GO are assigned to the stretching vibrations of carboxyl C=O, C=C and alkoxy C—O [38], respectively. The broad absorption at 3300–3600 cm^{-1} is attributed to the O—H stretching vibration, and the band at 1385 cm^{-1} is ascribed to the bending mode of O—H groups [39]. All the Ag_3PO_4 -based samples have similar FTIR peaks at 1010 and 550 cm^{-1} , which are ascribed to P—O stretching vibrations of PO_4^{3-} [40]. In contrast to the spectrum of Ag_3PO_4/GO , the peak intensity of C=O (1670 cm^{-1}) and alkoxy C—O (1058 cm^{-1}) decrease while that of C=C (1600 cm^{-1}) increases evidently in the spectra of $Ag_3PO_4/RGO/Ag$. This indicates the removal of oxygen-containing functional groups and the partially reduction of GO in $Ag_3PO_4/RGO/Ag$. Additionally, the C=O and C=C absorption peaks in $Ag_3PO_4/RGO/Ag$ shift to lower wavenumbers compared to that of GO, suggesting the existence of charge interaction between Ag_3PO_4 and RGO in the composites [41]. Fig. 2(b) illustrates the Raman spectra of the photocatalysts. In the spectra of Ag_3PO_4 and Ag/Ag_3PO_4 , three distinct Raman peaks at 410, 575 and 720 cm^{-1} are ascribed to the symmetric stretch of P—O—P bonds, and the strong peak at 903 cm^{-1} is arising from the motion of terminal oxygen bond vibration in phosphate chains [42]. The Raman spectrum of GO shows two characteristic peaks, namely, the D band at 1355 cm^{-1} and the G band at 1600 cm^{-1} . The D band is ascribed to edge or in-plane sp^3 defects and disordered carbon, whereas the G band arises from the in-plane vibration of ordered sp^2 -bonded carbon atoms in a two dimensional hexagonal lattice [43]. Hence, the intensity ratio of the D and G bands (I_D/I_G) is often used to evaluate the disorder degree in the graphitic layers. Compared with the GO sheets, the value of I_D/I_G in Ag_3PO_4/GO increased from 1.210 to 1.567, indicating that more defects were introduced in the GO layers by the incorporation of Ag_3PO_4 nanoparticles. The Raman spectrum of $Ag_3PO_4/RGO/Ag$ is similar to that of Ag_3PO_4/GO , but

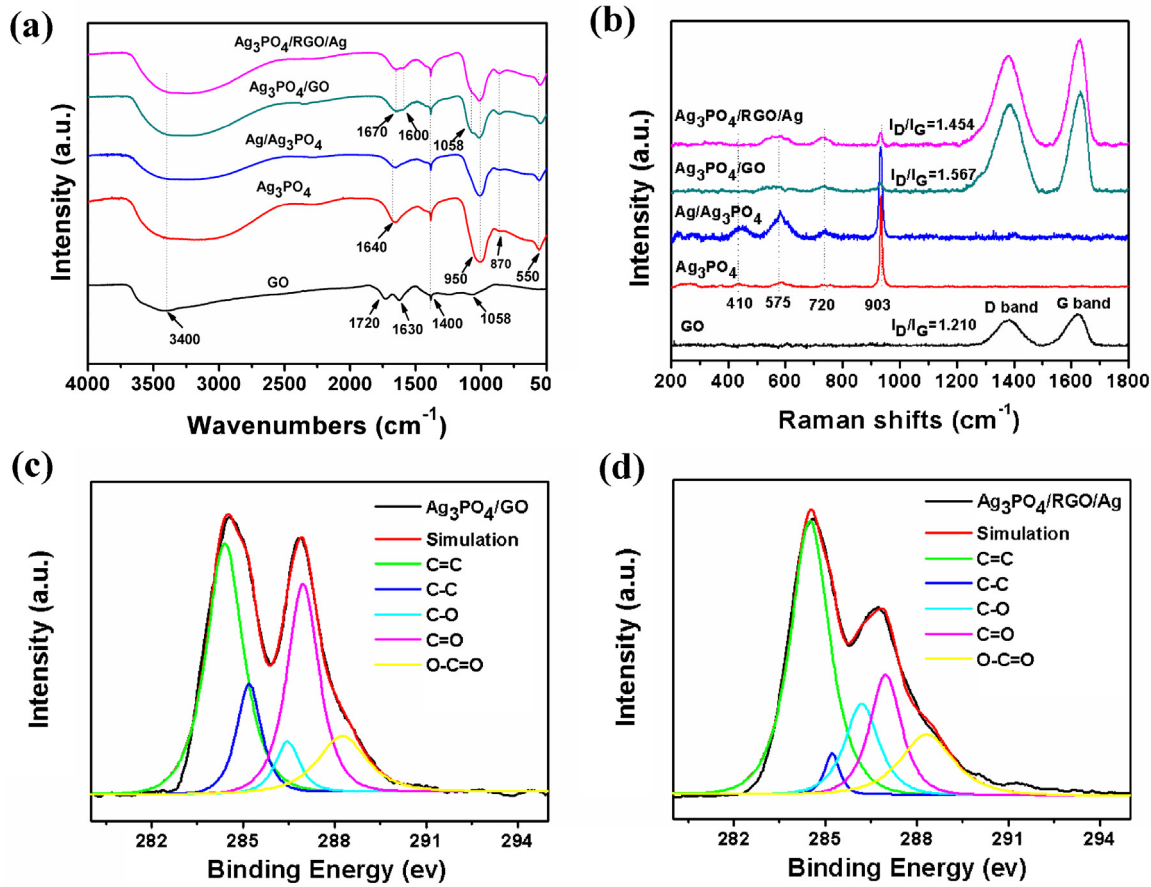


Fig. 2. (a) FTIR spectra and (b) Raman spectra of GO, Ag_3PO_4 , $\text{Ag/Ag}_3\text{PO}_4$, $\text{Ag}_3\text{PO}_4/\text{GO}$, and $\text{Ag}_3\text{PO}_4/\text{RGO/Ag}$; The C1s XPS spectra of (c) $\text{Ag}_3\text{PO}_4/\text{GO}$ and (d) $\text{Ag}_3\text{PO}_4/\text{RGO/Ag}$.

the value of I_D/I_G shifts downward to 1.454, demonstrating that the GO sheets in $\text{Ag}_3\text{PO}_4/\text{GO}$ have been partially reduced into RGO after photoreduction. It is notable that the $\text{Ag}_3\text{PO}_4/\text{RGO/Ag}$ composites in our work still show a relative higher I_D/I_G ratio than the GO owing to the strong interaction between the plasmonic Ag nanocrystals and RGO sheets, which is beneficial to the effective separation and transfer of photogenerated electrons and holes in photocatalysis.

The C1s XPS spectra of the $\text{Ag}_3\text{PO}_4/\text{GO}$ and $\text{Ag}_3\text{PO}_4/\text{RGO/Ag}$ were further measured to confirm the photoreduction of GO into RGO [Fig. 2(c) and (d)]. The high-resolution C1s spectra can be divided into five different peaks at 284.6, 285.0, 286.6, 287.8, and 288.4 eV. The peaks at 284.6 and 285.0 eV can be assigned to $\text{C}=\text{C}$ and $\text{C}-\text{C}$, while the other three peaks at 286.6, 287.8, and 288.4 eV can be assigned to $\text{C}-\text{O}$, $\text{C}=\text{O}$, and $\text{O}-\text{C}=\text{O}$, respectively [44]. After photoreduction, the peaks related to $\text{C}-\text{O}$, $\text{C}=\text{O}$, and $\text{O}-\text{C}=\text{O}$ are still observed in the XPS spectrum of $\text{Ag}_3\text{PO}_4/\text{RGO/Ag}$ [Fig. 2(d)], however, the percentage of these oxygen-containing functional groups decreases in large degree compared to that in $\text{Ag}_3\text{PO}_4/\text{GO}$ [Fig. 2(c)], indicating that the photoreduction of GO into RGO was successfully realized.

The morphology and microstructure of the as-prepared photocatalysts were studied by SEM and TEM, as shown in Figs. 3 and 4. In Fig. 3(a), the bare Ag_3PO_4 nanoparticles reveal regular spherical shapes with an average diameter of 200 nm. Similar Ag_3PO_4 nanospheres are observed in $\text{Ag/Ag}_3\text{PO}_4$ except for the appearance of many Ag nanoparticles with size of about 20 nm on the surface of Ag_3PO_4 [Fig. 3(b)]. In the SEM image of $\text{Ag}_3\text{PO}_4/\text{GO}$ [Fig. 3(c)], Ag_3PO_4 nanospheres are enwrapped by wrinkled and gauze-like GO sheets. The SEM image of $\text{Ag}_3\text{PO}_4/\text{RGO/Ag}$ in Fig. 3(d) shows a similar morphology as that of $\text{Ag}_3\text{PO}_4/\text{GO}$. Although some tiny

metallic Ag nanoparticles can also be observed on the surface of Ag_3PO_4 nanoparticles in Fig. 3(d), but the density is much lower than that in $\text{Ag/Ag}_3\text{PO}_4$. Fig. 4 shows the TEM images of the photocatalysts. The bare Ag_3PO_4 nanospheres are approximately 200 nm in diameter [Fig. 4(a)], which is consistent with the SEM result. As for $\text{Ag/Ag}_3\text{PO}_4$ sample [Fig. 4(b)], besides the Ag_3PO_4 nanospheres, many Ag nanoparticles with dark contrast are observed on the surface of Ag_3PO_4 . The existence of tiny Ag nanoparticles is confirmed by the HRTEM image in Fig. S1. The lattice spacing of 0.238 nm, corresponding to the d -spacing of (111) crystallographic plane of metallic Ag, can be observed in $\text{Ag/Ag}_3\text{PO}_4$ [Fig. S1(b)] and $\text{Ag}_3\text{PO}_4/\text{RGO/Ag}$ [Fig. S1(d)]. In Fig. 4(c), the light-gray regions in the TEM image of $\text{Ag}_3\text{PO}_4/\text{GO}$ are the crumpled GO sheets, and the dark regions are Ag_3PO_4 nanospheres. It is clearly observed that the Ag_3PO_4 nanospheres are firmly enwrapped by GO sheets even after extensive rinsing and sonication, which are applied for dispersing powder samples in ethanol before TEM characterization, indicating the strong chemical bonding between Ag_3PO_4 nanospheres and GO sheets. The TEM image of $\text{Ag}_3\text{PO}_4/\text{RGO/Ag}$ in Fig. 4(d) displays a novel hybrid structure different from that of $\text{Ag}_3\text{PO}_4/\text{GO}$. The RGO sheets that enwrap Ag_3PO_4 nanospheres are decorated with high density dispersive Ag nanoparticles. It is notable that although a few tiny metallic Ag nanoparticles can also be observed on the surface of Ag_3PO_4 nanoparticles in $\text{Ag}_3\text{PO}_4/\text{RGO/Ag}$, but their density is almost negligible compared to that on the RGO surface, indicating that the Ag nanoparticles were selectively grown on RGO during photoreduction. Furthermore, the density of Ag nanoparticles observed on the surface of Ag_3PO_4 nanoparticles in $\text{Ag}_3\text{PO}_4/\text{RGO/Ag}$ is much lower than that in $\text{Ag/Ag}_3\text{PO}_4$. Figs. 4(e) and (f) show the HRTEM images of the RGO sheets in $\text{Ag}_3\text{PO}_4/\text{RGO/Ag}$. A large

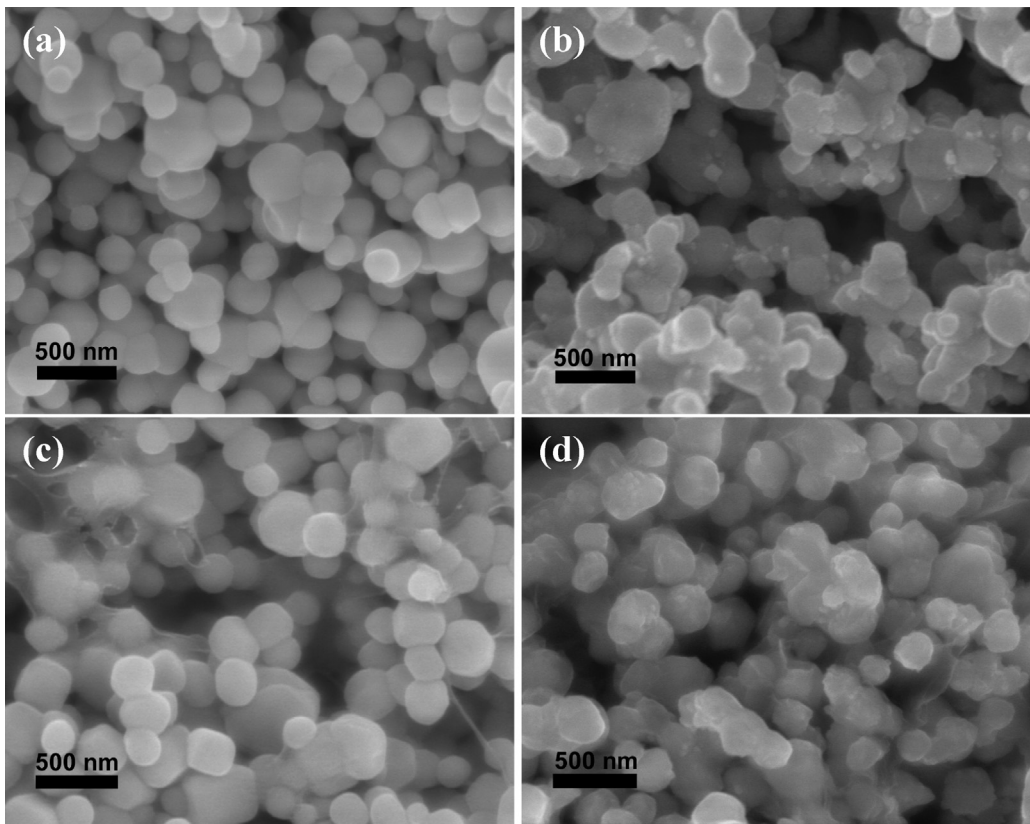
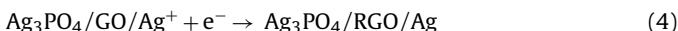
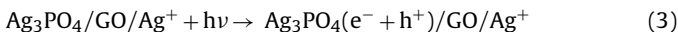


Fig. 3. SEM images of (a) Ag_3PO_4 , (b) $\text{Ag}/\text{Ag}_3\text{PO}_4$, (c) $\text{Ag}_3\text{PO}_4/\text{GO}$, and (d) $\text{Ag}_3\text{PO}_4/\text{RGO}/\text{Ag}$.

amount of nanoparticles with diameters of 5–10 nm are observed uniformly on the surface of the RGO [Fig. 4(e)]. The lattice spacing (0.238 nm) of the nanoparticles agrees with the *d*-spacing of (111) plane of the cubic Ag phase [Fig. 4(f)], confirming that the nanoparticles on the RGO sheets are indeed Ag nanocrystals. Herein, we demonstrate the successfully synthesis of the novel $\text{Ag}_3\text{PO}_4/\text{RGO}/\text{Ag}$ hybrid structure, which consists of $\text{Ag}_3\text{PO}_4/\text{RGO}$ with close interfacial contact and well dispersive Ag nanocrystals on the RGO sheets.

3.2. Formation mechanism of $\text{Ag}_3\text{PO}_4/\text{RGO}/\text{Ag}$

Based on the above experimental results, the synthesis process of $\text{Ag}_3\text{PO}_4/\text{RGO}/\text{Ag}$ nanocomposite is proposed and schematically illustrated in Fig. 5. The reactions involved in the synthesis are summarized as follows:



The overall synthesis can be divided into four consecutive stages. First, when AgNO_3 is dissolved in the GO aqueous solution, positively charged Ag^+ can be uniformly absorbed on the surface of GO sheets, which is negatively charged due to the existence of oxygen-containing functional groups (Eq. (1)). Second, when PO_4^{3-} is slowly released from HPO_4^{2-} , the Ag^+ react with PO_4^{3-} to form Ag_3PO_4 nanoparticles on the surface of GO (Eq. (2)). Since the Na_2HPO_4 is insufficient in the reaction, there are still many residual Ag^+ absorbed on the surface of GO after reaction ($\text{Ag}_3\text{PO}_4/\text{GO}/\text{Ag}^+$). Third, when the $\text{Ag}_3\text{PO}_4/\text{GO}/\text{Ag}^+$ is exposed to the visible-light irradiation in ethanol solution, photoexcited electron-hole pairs are

generated in Ag_3PO_4 (Eq. (3)). Finally, the residual Ag^+ and GO are reduced into metallic Ag nanocrystals and RGO simultaneously by accepting photoelectrons from the conduction band of Ag_3PO_4 (Eq. (4)), while the ethanol acts as a hole scavenger in the photoreduction [28]. As a result, the novel $\text{Ag}_3\text{PO}_4/\text{RGO}/\text{Ag}$ hybrid structure consists of $\text{Ag}_3\text{PO}_4/\text{RGO}$ with close interfacial contact and well dispersive Ag nanocrystals on RGO sheets are obtained. Since most of the photo-generated electrons are consumed by the Ag^+ and GO, the photocorrosion of Ag_3PO_4 under light irradiation can be strongly inhibited and thus only a small load of Ag nanoparticles can be found on the surface of Ag_3PO_4 nanospheres.

3.3. Optical absorption properties of photocatalysts

The optical absorption properties of the photocatalysts were studied by UVDRS spectra. As shown in Fig. 6(a), bare Ag_3PO_4 exhibits strong absorbance in wavelengths shorter than 530 nm, corresponding to its band-gap energy of 2.36 eV [45]. Compared to bare Ag_3PO_4 , a stronger absorption in the visible-light region is observed in $\text{Ag}/\text{Ag}_3\text{PO}_4$ due to the existence of excess Ag nanoparticles on the surface of Ag_3PO_4 . The $\text{Ag}_3\text{PO}_4/\text{GO}$ shows much stronger visible light absorption than the bare Ag_3PO_4 due to the incorporation of GO sheets [19]. $\text{Ag}_3\text{PO}_4/\text{RGO}/\text{Ag}$ exhibits the strongest absorption in the visible light range of 530–800 nm. It might be ascribed to the SPR effect of Ag nanocrystals on RGO and the restoring of the electronic conjugation within the RGO sheet [46]. The enhancement due to increased scattering of Ag nanocrystals is negligible, because significant light scattering are only seen in large plasmonic Ag nanoparticles (above 50 nm) [47]. According to the Kubelka–Munk function [48], the relation between absorption coefficient and the band-gap energy of semiconductor can be described by the equation $\alpha h\nu = A(h\nu - E_g)^{n/2}$, where α , ν and A are diffuse reflection absorption coefficient, light frequency and

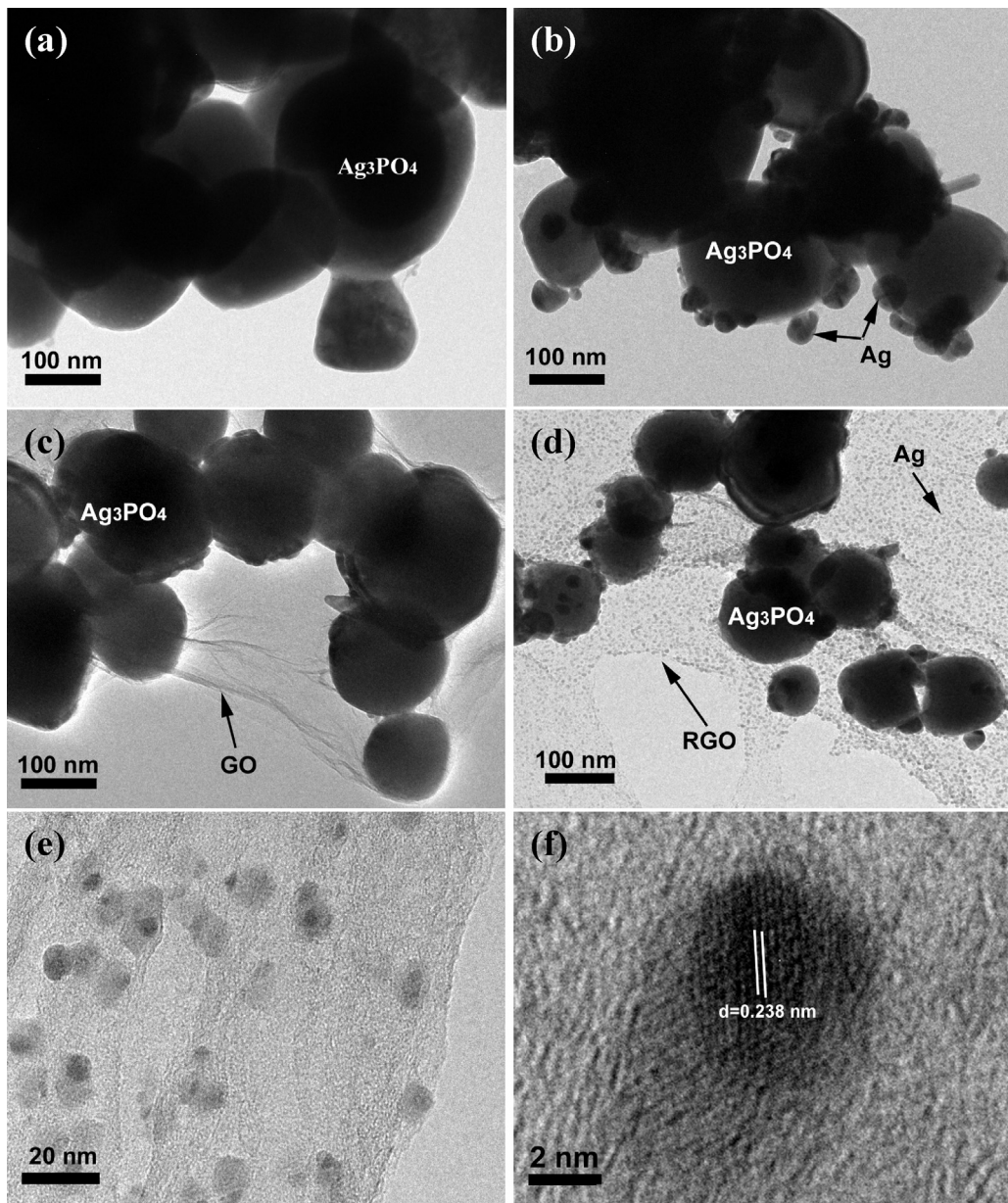


Fig. 4. TEM images of (a) Ag_3PO_4 , (b) $\text{Ag}/\text{Ag}_3\text{PO}_4$, (c) $\text{Ag}_3\text{PO}_4/\text{GO}$, (d) $\text{Ag}_3\text{PO}_4/\text{RGO}/\text{Ag}$; HRTEM images of (e) RGO and (f) Ag nanocrystals in $\text{Ag}_3\text{PO}_4/\text{RGO}/\text{Ag}$.

proportionality constant, respectively. From the plot of $(\alpha h\nu)^2$ versus E_g in Fig. 6(b), the transition band-gaps estimated from the onset of the curve edges are about 2.36, 2.31, 2.25 and 2.16 eV for Ag_3PO_4 , $\text{Ag}/\text{Ag}_3\text{PO}_4$, $\text{Ag}_3\text{PO}_4/\text{GO}$, $\text{Ag}_3\text{PO}_4/\text{RGO}/\text{Ag}$, respectively. The relatively narrow band-gap energy observed for $\text{Ag}_3\text{PO}_4/\text{RGO}/\text{Ag}$ may be ascribed to the strong interaction in the hybrid structure [49], which makes the utilization of the solar spectrum more efficient.

3.4. Photocatalytic performance and photostability under visible light

The photocatalytic performance of $\text{Ag}_3\text{PO}_4/\text{RGO}/\text{Ag}$ was evaluated by degradation of RhB and phenol aqueous solution under visible light without adding any sacrificial reagents. Ag_3PO_4 , $\text{Ag}/\text{Ag}_3\text{PO}_4$, and $\text{Ag}_3\text{PO}_4/\text{GO}$ were also studied under the same condition for comparison. Fig. 7(a) shows the photocatalytic degradation curves of RhB as a function of time. Before light

irradiation, the solution of RhB and photocatalyst was magnetically stirred in dark for 30 min to establish an adsorption–desorption equilibrium. The decrease of the RhB concentration due to the adsorption of $\text{Ag}_3\text{PO}_4/\text{GO}$ or $\text{Ag}_3\text{PO}_4/\text{RGO}/\text{Ag}$ (about 8%) is higher than that of Ag_3PO_4 or $\text{Ag}/\text{Ag}_3\text{PO}_4$ (about 2%), indicating that GO or RGO in the composites can enhance the absorption of organic molecules on the surface of photocatalysts. The enhanced adsorptivity is mainly attributed to the π – π stacking and electrostatic attraction between RhB and aromatic regions of the high-surface-area graphene [50]. Under visible-light irradiation, the photocatalytic performance of different photocatalysts follows the order of $\text{Ag}/\text{Ag}_3\text{PO}_4 < \text{Ag}_3\text{PO}_4 < \text{Ag}_3\text{PO}_4/\text{GO} < \text{Ag}_3\text{PO}_4/\text{RGO}/\text{Ag}$. The apparent rate constants (k) calculated from the degradation curves of $-\ln(C/C_0)$ versus irradiation time are 0.0280, 0.0144, 0.1029, 0.1411 min^{-1} for Ag_3PO_4 , $\text{Ag}/\text{Ag}_3\text{PO}_4$, $\text{Ag}_3\text{PO}_4/\text{GO}$ and $\text{Ag}_3\text{PO}_4/\text{RGO}/\text{Ag}$ [Fig. 7(b)], respectively. The photocatalytic rate of $\text{Ag}_3\text{PO}_4/\text{RGO}/\text{Ag}$ is about 5 times that of Ag_3PO_4 nanoparticles. In addition to RhB, phenol was also used as

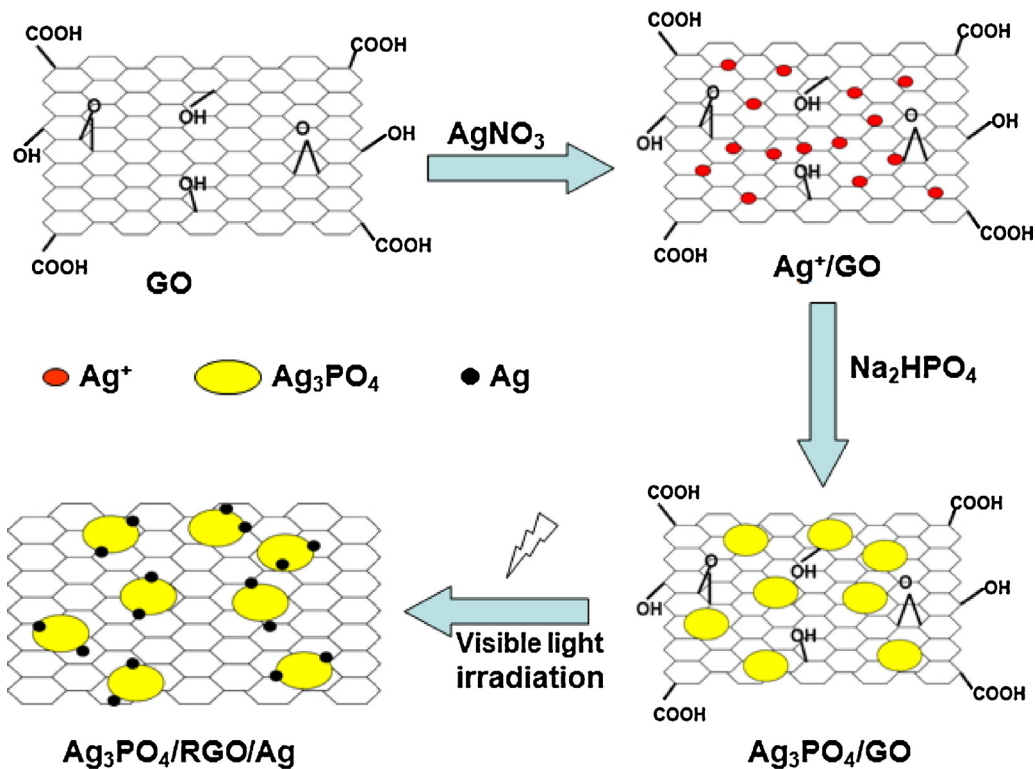


Fig. 5. The schematic illustration of the synthesis process of $\text{Ag}_3\text{PO}_4/\text{RGO}/\text{Ag}$.

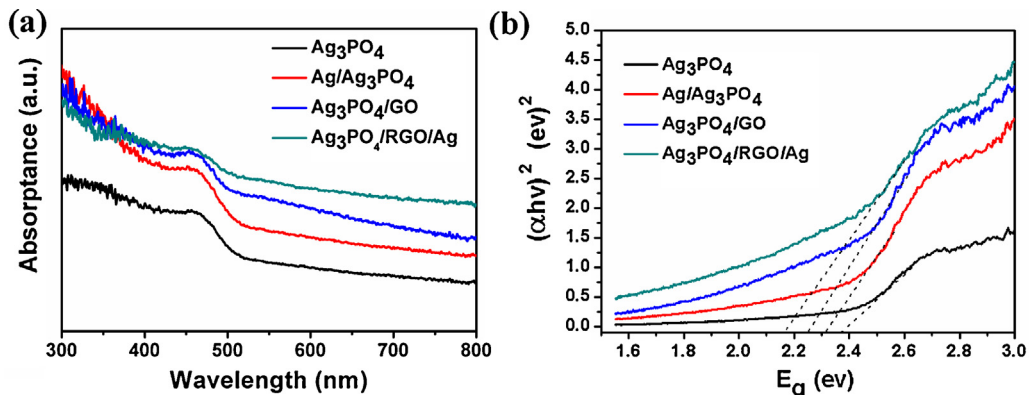


Fig. 6. (a) UVDRS spectra of Ag_3PO_4 , $\text{Ag}/\text{Ag}_3\text{PO}_4$, $\text{Ag}_3\text{PO}_4/\text{GO}$, and $\text{Ag}_3\text{PO}_4/\text{RGO}/\text{Ag}$, (b) the plot of $(\alpha h\nu)^2$ versus E_g .

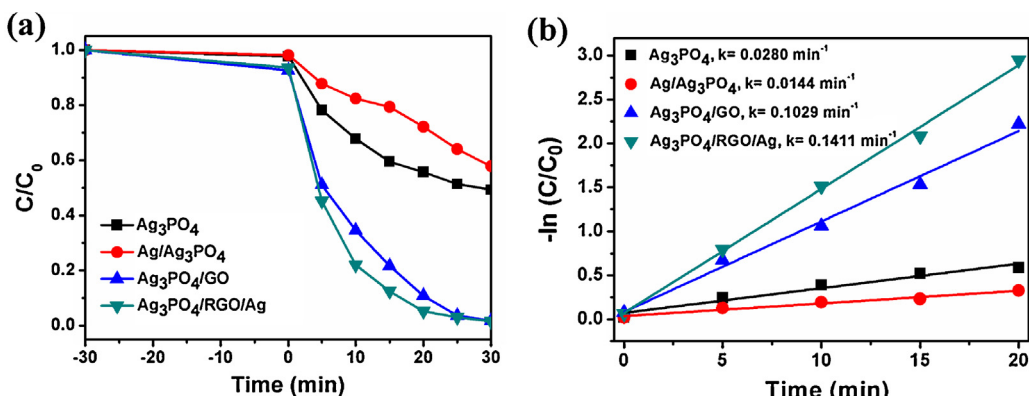


Fig. 7. (a) RhB photodegradation as a function of illumination time for Ag_3PO_4 , $\text{Ag}/\text{Ag}_3\text{PO}_4$, $\text{Ag}_3\text{PO}_4/\text{GO}$, and $\text{Ag}_3\text{PO}_4/\text{RGO}/\text{Ag}$; (b) The plots of $-\ln(C/C_0)$ versus t . C_0 is the initial concentration of RhB before light irradiation and C is the concentration at irradiation time t .

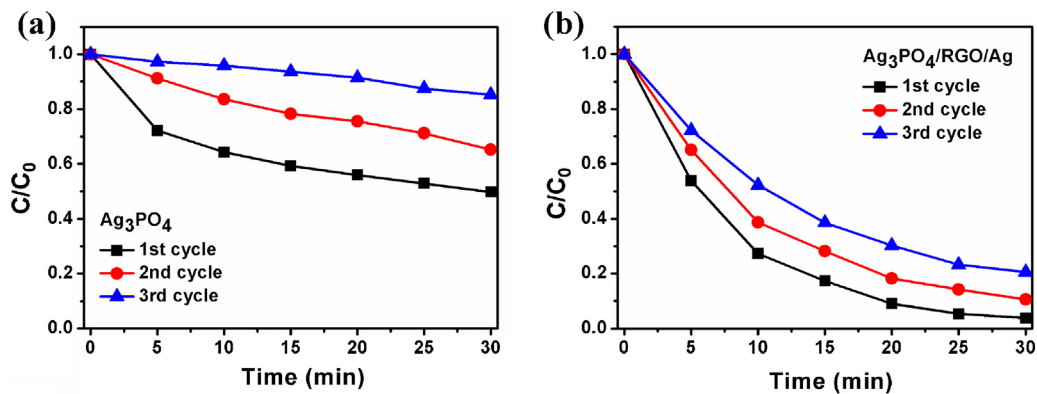


Fig. 8. Plots of cycling photodegradation of RhB by (a) Ag_3PO_4 and (b) $\text{Ag}_3\text{PO}_4/\text{RGO/Ag}$ under visible light.

a persistent organic pollutant to evaluate the photocatalytic performance of $\text{Ag}_3\text{PO}_4/\text{RGO/Ag}$. The change of the residual concentration of phenol was measured with HPLC [Fig. S2(b)], and the photodegradation of RhB was also measured with the same method for comparison [Fig. S2(a)]. It is obviously that the photocatalytic performance of different photocatalysts for both phenol and RhB degradations follows the same order of $\text{Ag}/\text{Ag}_3\text{PO}_4 < \text{Ag}_3\text{PO}_4 < \text{Ag}_3\text{PO}_4/\text{GO} < \text{Ag}_3\text{PO}_4/\text{RGO/Ag}$, even though the degradation of phenol is more difficult than that of RhB. After 30 min irradiation, the residual concentrations of RhB decreased from 20 mg/L to 4.1, 6.5, 2.2, 1.9 mg/L when Ag_3PO_4 , $\text{Ag}/\text{Ag}_3\text{PO}_4$, $\text{Ag}_3\text{PO}_4/\text{GO}$ or $\text{Ag}_3\text{PO}_4/\text{RGO/Ag}$ was used as photocatalyst, respectively. As for the degradation of phenol, the residual concentration decreased quickly at the early stage of reaction for all the photocatalyst but slowed down after 15 min, indicating that completed decomposition of the phenol need long time. The poor photocatalytic activity of $\text{Ag}/\text{Ag}_3\text{PO}_4$ in our experiment is ascribed to the formation of excess Ag nanoparticles on the surface of Ag_3PO_4 , which is consistent with other reports that the photocatalytic activity of $\text{Ag}/\text{Ag}_3\text{PO}_4$ would decrease at a high level of metallic silver coverage on Ag_3PO_4 surface [29,31].

In addition to photocatalytic activity, the stability of photocatalysts is another important issue in practical application. In order to investigate the stability of the photocatalysts, three runs of cycling photodegradation experiments under the identical condition have been carried out for bare Ag_3PO_4 and $\text{Ag}_3\text{PO}_4/\text{RGO/Ag}$ [Fig. 8]. The photocatalytic performance of Ag_3PO_4 decreases evidently after the cycling degradation experiments [Fig. 8(a)], while $\text{Ag}_3\text{PO}_4/\text{RGO/Ag}$ still maintains a high level of activity [Fig. 8(b)]. The morphologies of the final photocatalysts after cycling experiments are shown in Fig. S3. There is no obvious change in the morphology of $\text{Ag}_3\text{PO}_4/\text{RGO/Ag}$ after repeated photocatalysis experiment [Fig. S3(b)], whereas the Ag_3PO_4 sample aggregated into larger particles and the particles surface was covered with many Ag nanoparticles [Fig. S3(a)]. It is thus evident that the construction of $\text{Ag}_3\text{PO}_4/\text{RGO/Ag}$ heterostructure not only prevents the photocorrosion of Ag_3PO_4 but also prohibits the agglomeration of Ag_3PO_4 particles. As a result, the $\text{Ag}_3\text{PO}_4/\text{RGO/Ag}$ exhibits superior stability to bare Ag_3PO_4 in photocatalysis.

3.5. Mechanism for the improved photocatalytic activity and stability of $\text{Ag}_3\text{PO}_4/\text{RGO/Ag}$

The above experimental results and discussions demonstrate that the photocatalytic activity and stability of Ag_3PO_4 can be improved in a large degree via coupling Ag_3PO_4 with RGO sheets decorated with Ag nanocrystals. This should be mainly attributed to the fast separation and transfer of photo-generated charges in the heterostructure. PL spectra are useful to disclose the

migration, transfer, and recombination processes of the photo-generated electron–hole pairs in semiconductors. Fig. 9 shows the PL spectra of the photocatalysts, in which the Ag_3PO_4 emission is similar to the previous report [51]. The significant quenching of the Ag_3PO_4 emission in $\text{Ag}_3\text{PO}_4/\text{RGO/Ag}$ compared to those of other photocatalysts indicates that the recombination of photo-generated electron–hole pairs in Ag_3PO_4 has been effectively suppressed in the heterostructure. It is also noticed that the PL emission of $\text{Ag}/\text{Ag}_3\text{PO}_4$ also decreases evidently when compared with that of bare Ag_3PO_4 . This can be explained by the excess Ag nanoparticles on the surface of Ag_3PO_4 in $\text{Ag}/\text{Ag}_3\text{PO}_4$, as shown in the TEM image of Fig. 4(b). Under visible light irradiation, a portion of the incident light was absorbed by the excess Ag nanoparticles instead of Ag_3PO_4 in $\text{Ag}/\text{Ag}_3\text{PO}_4$ [29,31]. Therefore, the weaker PL emission observed for $\text{Ag}/\text{Ag}_3\text{PO}_4$ should be ascribed to two factors: less photo-generated electron–hole pairs in Ag_3PO_4 due to the shade of incident light by Ag nanoparticles and the suppressed electron–hole recombination due to the electron transfer from Ag_3PO_4 to Ag. Since the excess Ag nanoparticles on the surface of Ag_3PO_4 would prevent visible light absorption by Ag_3PO_4 and inevitably cover active sites for photocatalysis, the $\text{Ag}/\text{Ag}_3\text{PO}_4$ exhibited a relatively weaker photocatalytic activity than bare Ag_3PO_4 (Fig. 7) [29,31]. As for $\text{Ag}_3\text{PO}_4/\text{RGO/Ag}$, most of the Ag nanocrystals are selectively decorated on RGO rather than on the surface of Ag_3PO_4 , so the Ag nanocrystals have little influence on the excitation of Ag_3PO_4 by the incident light. Therefore, the only reason for the quenched PL emission in $\text{Ag}_3\text{PO}_4/\text{RGO/Ag}$ is the suppressed recombination of photo-generated electron–hole pairs. The transient photocurrent responses of the photocatalyst photoanodes under visible-light irradiation were also measured and

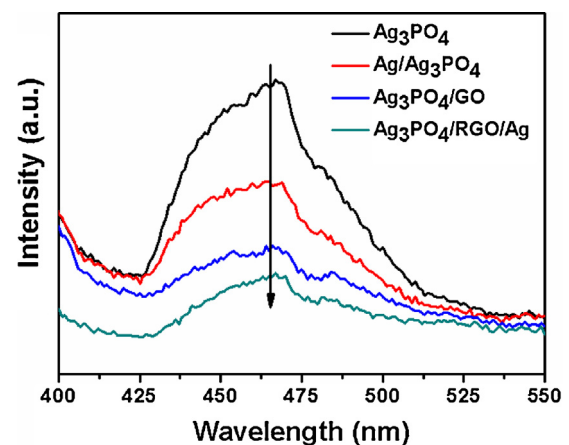


Fig. 9. PL spectra of Ag_3PO_4 , $\text{Ag}/\text{Ag}_3\text{PO}_4$, $\text{Ag}_3\text{PO}_4/\text{GO}$, and $\text{Ag}_3\text{PO}_4/\text{RGO/Ag}$.

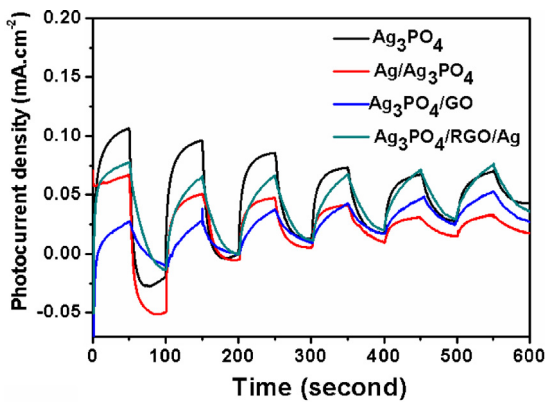


Fig. 10. The transient photocurrent response of Ag_3PO_4 , $\text{Ag}/\text{Ag}_3\text{PO}_4$, $\text{Ag}_3\text{PO}_4/\text{GO}$, and $\text{Ag}_3\text{PO}_4/\text{RGO}/\text{Ag}$ electrodes.

shown in Fig. 10. Since the photocurrent of the photoanodes prepared by a doctor-blade method can be influenced by several factors, such as the amount of photocatalyst, the contact between photocatalyst and FTO glass and the light pathway in the photoanodes, the photocurrent density cannot directly reflect the whole photochemical properties of different photocatalysts. However, their reproducibility can reflect the stability of photocatalysts during the photoelectrochemical process. In Fig. 10, the bare Ag_3PO_4 photoanode shows a high photocurrent density of about $0.10 \text{ mA}/\text{cm}^2$ at the beginning of irradiation, but the photocurrent density decreases rapidly after six cycles of irradiation. The $\text{Ag}_3\text{PO}_4/\text{RGO}/\text{Ag}$ is the most stable sample among the four photocatalysts and its photocurrent density remains at about $0.07 \text{ mA}/\text{cm}^2$ in the whole experiment. The $\text{Ag}_3\text{PO}_4/\text{GO}$ exhibits the second stable photocurrent density, while the stability of the $\text{Ag}/\text{Ag}_3\text{PO}_4$ is the worst. Moreover, after 10 min light irradiation, the $\text{Ag}_3\text{PO}_4/\text{RGO}/\text{Ag}$ exhibited the highest photocurrent and the $\text{Ag}/\text{Ag}_3\text{PO}_4$ exhibited the lowest photocurrent, which are in consistent with the photocatalytic activities of the samples. The PL and transient photocurrent response experiment demonstrate that the coupling of RGO decorated with Ag nanocrystals can significantly enhance the separation and transfer of photoexcited charge carriers and finally improve the photocatalytic activity and stability of Ag_3PO_4 photocatalyst.

Furthermore, reactive oxidative species trapping experiments were performed to investigate the main reactive oxidative species involved in the photocatalytic process by using three different scavengers, *p*-benzoquinone (BQ, $\text{O}_2\bullet^-$ radicals scavenger), disodium ethylenediaminetetraacetate (EDTA, holes scavenger) and isopropanol (IPA, $\text{OH}\bullet$ radicals scavenger). Similar to previous report [10,21], when bare Ag_3PO_4 was used as photocatalyst [Fig. 11(a)],

the photodegradation of RhB were significantly suppressed by the introduction of EDTA anions, indicating that holes are the main reactive oxidative species involved in the photocatalysis. In contrast, the adding of BQ or IPA in the solution has no obvious effect on the photocatalytic activity of Ag_3PO_4 [Fig. 11(a)], implying that $\text{O}_2\bullet^-$ radicals and $\text{OH}\bullet$ radicals have no contribution to the degradation process. The photocatalytic behavior of $\text{Ag}_3\text{PO}_4/\text{RGO}/\text{Ag}$ is similar to that of bare Ag_3PO_4 when EDTA or IPA was introduced into the photoreaction [Fig. 11(b)]. However, the adding of BQ results in an unneglectable deactivation of $\text{Ag}_3\text{PO}_4/\text{RGO}/\text{Ag}$, indicating that besides holes, $\text{O}_2\bullet^-$ radicals are also involved in the photocatalytic process.

It is known that the valence band edge potential (2.81 eV) of Ag_3PO_4 is close to E^θ ($\text{OH}\bullet/\text{H}_2\text{O}$) (2.68 eV) and the conduction band edge potential (0.45 eV) is less negative than E^θ ($\text{O}_2/\text{O}_2\bullet^-$) (0.13 eV). It means that it is difficult for holes to directly oxidize H_2O molecules into $\text{OH}\bullet$ radicals, and electrons cannot directly reduce O_2 molecules into $\text{O}_2\bullet^-$ radicals in pure Ag_3PO_4 [10]. However, there exist high density plasmonic Ag nanocrystals on the surface of RGO in $\text{Ag}_3\text{PO}_4/\text{RGO}/\text{Ag}$. When $\text{Ag}_3\text{PO}_4/\text{RGO}/\text{Ag}$ was subjected to light irradiation, the photo-induced separation of electrons and holes arises from the dipolar character of the SPR effect of Ag nanocrystals [52,53]. The active photo-induced electrons in Ag nanocrystals could reduce O_2 molecules to form $\text{O}_2\bullet^-$ radicals [54,55], leaving behind holes (Ag^+) that is filled by electrons from Ag_3PO_4 via conductive RGO. Because the conduction band of RGO are more positive than the conduction band edge of Ag_3PO_4 [22], the photo-generated electrons in Ag_3PO_4 can be captured by RGO and then quickly shuttled across the two-dimensional carbon network to Ag nanocrystal sites. As a result, the Ag nanocrystals on RGO not only promote the electronic conductivity of RGO but also facilitate the generation of additional active species for photocatalytic redox reaction.

On the basis of above experimental results and discussion, the possible mechanism for photocatalytic degradation of organic pollutants by $\text{Ag}_3\text{PO}_4/\text{RGO}/\text{Ag}$ is proposed and schematically illustrated in Fig. 12. The relevant reactions are listed in Eqs. (5)–(10). Besides the electrons (e^-) and holes (h^+) generated in the photoexcited Ag_3PO_4 (Eq. (5)), electrons and holes can also be generated on the photoexcited plasmonic Ag (Ag^*) nanocrystals (Eq. (6)) due to the SPR effect under visible-light irradiation [56]. The active electrons generated on the plasmonic Ag nanocrystals react with O_2 to form $\text{O}_2\bullet^-$ radicals and result in the formation of Ag^+ simultaneously (Eq. (7)) [57]. Meanwhile, the photo-generated electrons in the conduction band (CB) of Ag_3PO_4 can be rapidly transferred along the $\pi-\pi$ graphitic network of RGO sheets (Eq. (8)) and captured by Ag^+ to regenerate Ag nanocrystals on the surface of RGO (Eq. (9)). The photo-generated holes in the valence band (VB) of

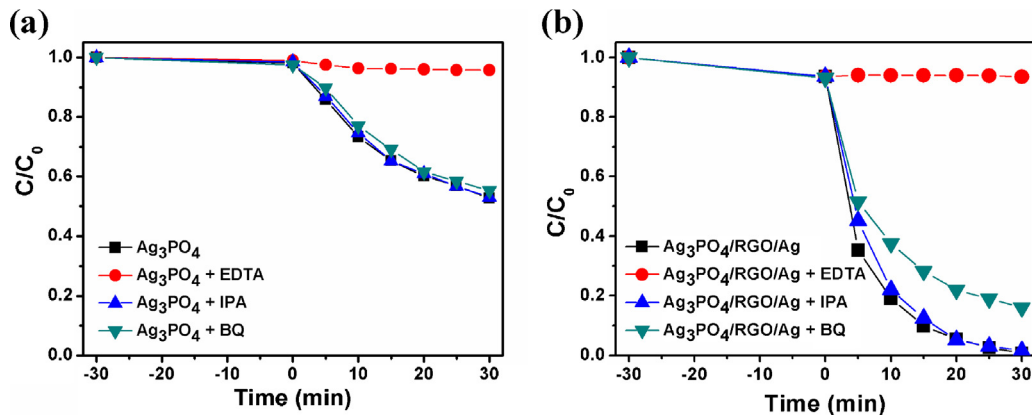


Fig. 11. Plots of photogenerated active species trapped in the system of photodegradation of RhB by (a) Ag_3PO_4 and (b) $\text{Ag}_3\text{PO}_4/\text{RGO}/\text{Ag}$ under visible light.

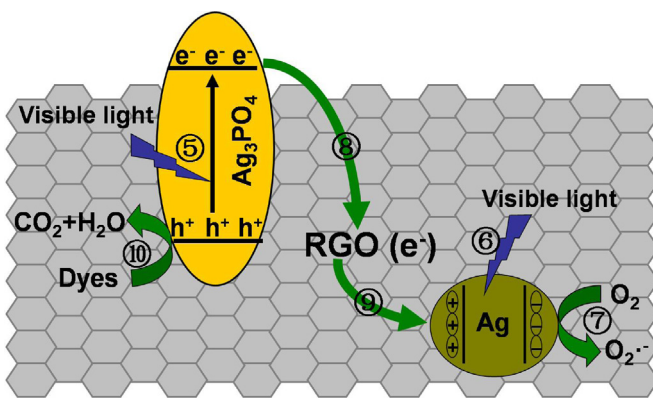
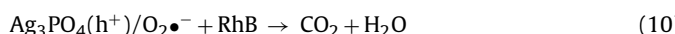
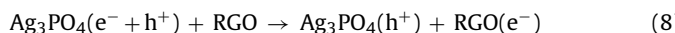
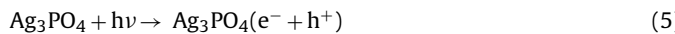


Fig. 12. The proposed mechanism for the photodegradation of organic molecules on the surface of $\text{Ag}_3\text{PO}_4/\text{RGO}/\text{Ag}$ nanocomposites.

Ag_3PO_4 together with $\text{O}_2\bullet^-$ radicals at Ag nanocrystals can oxidize organic dye directly (Eq. (10)). The novel electron transfer channel of $\text{Ag}_3\text{PO}_4 \rightarrow \text{RGO} \rightarrow \text{Ag}$, which results in the efficient separation of photo-generated electron–hole pairs, the inhabitation of photocorrosion of Ag_3PO_4 to metallic Ag in the photocatalytic process, and the generation of additional reactive oxidation species of $\text{O}_2\bullet^-$, are beneficial to the enhanced photocatalytic activity and stability of $\text{Ag}_3\text{PO}_4/\text{RGO}/\text{Ag}$. In addition, the strong adsorption ability of graphene for organic molecule, the relative narrow band-gap as well as the increasing absorbance in the visible light region also contribute to the improved photocatalytic activity of $\text{Ag}_3\text{PO}_4/\text{RGO}/\text{Ag}$ [58].



4. Conclusions

In summary, a novel $\text{Ag}_3\text{PO}_4/\text{RGO}/\text{Ag}$ heterostructure has been synthesized using a facile photo-assisted reduction method. The $\text{Ag}_3\text{PO}_4/\text{RGO}/\text{Ag}$ exhibited superior photocatalytic activity and stability to bare Ag_3PO_4 , $\text{Ag}/\text{Ag}_3\text{PO}_4$ and $\text{Ag}_3\text{PO}_4/\text{GO}$ under visible light. It is suggested the photo-generated electrons on Ag_3PO_4 can be quickly transferred to RGO sheets while RGO mainly act as electron acceptors and transfer channels in the heterostructure. Meanwhile, the photo-generated electrons at the plasmonic Ag nanocrystals can react with O_2 to form additional active species $\text{O}_2\bullet^-$ for photocatalysis, leaving behind holes (Ag^+) that is filled by electrons from Ag_3PO_4 via RGO. As a result, both the photocorrosion of Ag_3PO_4 and the recombination of electron–hole pairs in the photocatalyst are suppressed due to the fast separation and transfer of photo-generated electrons in $\text{Ag}_3\text{PO}_4/\text{RGO}/\text{Ag}$. In addition, the strong adsorption ability of graphene for organic molecule, the relative narrow band-gap and the increasing absorption in the visible-light region due to the SPR effect are also beneficial to the enhanced photocatalytic activity of $\text{Ag}_3\text{PO}_4/\text{RGO}/\text{Ag}$.

5. Supporting information

HRTEM of $\text{Ag}_3\text{PO}_4/\text{RGO}$, $\text{Ag}/\text{Ag}_3\text{PO}_4$, $\text{Ag}_3\text{PO}_4/\text{GO}$ and $\text{Ag}_3\text{PO}_4/\text{RGO}/\text{Ag}$; Photocatalytic degradation of RhB and

phenol under visible light; SEM images of Ag_3PO_4 and $\text{Ag}_3\text{PO}_4/\text{RGO}/\text{Ag}$ photocatalyst after cycling degradation experiments.

Acknowledgments

This work was supported by the National Natural Science Foundation of China (Nos. 60806045, 11074220), Open Foundation of Zhejiang Provincial Top Key Academic Discipline of Applied Chemistry, Eco-Dyeing & Finishing Engineering (No. YR2012008), 521 Talents Project of Zhejiang Sci-Tech University, Qianjiang Talents Program of Zhejiang Province (2013R10060), Xinmiao Undergraduate Student Talents Program of Zhejiang Province (2013R406037), and SRF for ROCS, SEM.

Appendix A. Supplementary data

Supplementary data associated with this article can be found, in the online version, at <http://dx.doi.org/10.1016/j.apcatb.2014.04.007>.

References

- [1] A. Kubacka, M. Fernandez-Garcia, G. Colon, *Chem. Rev.* 112 (2012) 1555–1614.
- [2] H. Tong, S.X. Ouyang, Y.P. Bi, N. Umezawa, M. Oshikiri, J.H. Ye, *Adv. Mater.* 24 (2012) 229–251.
- [3] P. Wang, B.B. Huang, X.Y. Qin, X.Y. Zhang, Y. Dai, J.Y. Wei, M.H. Whangbo, *Angew. Chem. Int. Ed.* 47 (2008) 7931–7933.
- [4] C. Hu, T.W. Peng, X.X. Hu, Y.L. Nie, X.F. Zhou, J.H. Qu, H. He, *J. Am. Chem. Soc.* 132 (2010) 857–862.
- [5] B. Wang, X.Q. Gu, Y.L. Zhao, Y.H. Qiang, *Appl. Surf. Sci.* 283 (2013) 396–401.
- [6] B. Chi, L. Zhao, T. Jin, *J. Phys. Chem. C* 111 (2007) 6189–6193.
- [7] H.B. Fu, C.S. Pan, W.Q. Yao, Y.F. Zhu, *J. Phys. Chem. B* 109 (2005) 22432–22439.
- [8] J.W. Tang, Z.G. Zou, J.H. Ye, *Angew. Chem. Int. Ed.* 43 (2004) 4463–4466.
- [9] Z.G. Yi, J.H. Ye, N. Kikugawa, T. Kako, S.X. Ouyang, H. Stuart-Williams, H. Yang, J.Y. Cao, W.J. Luo, Z.S. Li, Y. Liu, R.L. Withers, *Nat. Mater.* 9 (2010) 559–564.
- [10] Y.P. Bi, S.X. Ouyang, J.Y. Cao, J.H. Ye, *Phys. Chem. Chem. Phys.* 13 (2011) 10071–10075.
- [11] Y.P. Bi, S.X. Ouyang, N. Umezawa, J. Cao, J.H. Ye, *J. Am. Chem. Soc.* 133 (2011) 6490–6492.
- [12] Y.P. Liu, L. Fang, H.D. Lu, L.J. Liu, H. Wang, C.Z. Hu, *Catal. Commun.* 17 (2012) 200–204.
- [13] H. Wang, Y.S. Bai, J.T. Yang, X.F. Lang, J.H. Li, L. Guo, *Chem. Eur. J.* 18 (2012) 5524–5529.
- [14] J. Cao, B.D. Luo, H.L. Lin, B.Y. Xu, S.F. Chen, *J. Hazard. Mater.* 217–218 (2012) 107–115.
- [15] W.F. Yao, B. Zhang, C.P. Huang, C. Ma, X.L. Song, Q.J. Xu, *J. Mater. Chem.* 22 (2012) 4050–4055.
- [16] H.C. Zhang, H. Huang, H. Ming, H.T. Li, L.L. Zhang, Y. Liu, Z.H. Kang, *J. Mater. Chem.* 22 (2012) 10501–10506.
- [17] H.Y. Cui, X.F. Yang, Q.X. Gao, H. Liu, Y. Li, H. Tang, R.X. Zhang, J.L. Qin, X.H. Yan, *Mater. Lett.* 93 (2013) 28–31.
- [18] S. Bai, X.P. Shen, H.W. Lv, G.X. Zhu, C.L. Bao, Y.X. Shan, *J. Colloid Interface Sci.* 405 (2013) 1–9.
- [19] G.D. Chen, M. Sun, Q. Wei, Y.F. Zhang, B.C. Zhu, B. Du, *J. Hazard. Mater.* 244–245 (2013) 86–93.
- [20] Q.H. Liang, Y. Shi, W.J. Ma, Z. Li, X.M. Yang, *Phys. Chem. Chem. Phys.* 14 (2012) 15657–15665.
- [21] Y.H. Ao, P.F. Wang, C. Wang, J. Hou, J. Qian, *Appl. Surf. Sci.* 271 (2013) 265–270.
- [22] L. Liu, J.C. Liu, D.D. Sun, *Catal. Sci. Technol.* 2 (2012) 2525–2532.
- [23] P. Wu, Y.D. Qian, P. Du, H. Zhang, C.X. Cai, *J. Mater. Chem.* 22 (2012) 6402–6412.
- [24] M.J. McAllister, J. Li, D.H. Adamson, H.C. Schniepp, A.A. Abdala, J. Liu, M. Herrera-Alonso, D.L. Milius, R. Car, R.K. Prud'homme, I.A. Aksay, *Chem. Mater.* 19 (2007) 4396–4404.
- [25] J. Kauppinen, P. Kunnas, P. Damlin, A. Viinikanoja, C. Kvarnström, *Electrochim. Acta* 89 (2013) 84–89.
- [26] I.V. Lightcap, P.V. Kamat, *J. Am. Chem. Soc.* 134 (2012) 7109–7116.
- [27] G. Williams, B. Seger, P.V. Kamat, *ACS Nano* 2 (2008) 1487–1491.
- [28] G.Y. He, M.G. Qian, X.Q. Sun, Q. Chen, X. Wang, H.Q. Chen, *Powder Technol.* 246 (2013) 278–283.
- [29] M. Ge, N. Zhu, Y.P. Zhao, J. Li, L. Liu, *Ind. Eng. Chem. Res.* 51 (2012) 5167–5173.
- [30] Y.P. Bi, H.Y. Hu, S.X. Ouyang, G.X. Lu, J.Y. Cao, J.H. Ye, *Chem. Commun.* 48 (2012) 3748–3750.
- [31] M.A. Gondal, X.F. Chang, W.E.I. Sha, Z.H. Yamani, Q. Zhou, *J. Colloid Interface Sci.* 392 (2013) 325–330.
- [32] M.S. Zhu, P.L. Chen, M.H. Liu, *Langmuir* 29 (2013) 9259–9268.
- [33] X.F. Yang, H.Y. Cui, Y. Li, J.L. Qin, R.X. Zhang, H. Tang, *ACS Catal.* 3 (2013) 363–369.
- [34] D.C. Marcano, D.V. Kosynkin, J.M. Berlin, A. Sinitskii, Z.Z. Sun, A. Slesarev, L.B. Alemany, W. Lu, J.M. Tour, *ACS Nano* 4 (2010) 4806–4814.

[35] S. Park, J. An, J.R. Potts, A. Velamakanni, S. Murali, R.S. Ruoff, *Carbon* 49 (2011) 3019–3023.

[36] W. Fan, Q. Lai, Q. Zhang, Y. Wang, *J. Phys. Chem. C* 115 (2011) 10694.

[37] J.C. Liu, H.W. Bai, Y.J. Wang, Z.Y. Liu, X.W. Zhang, D.D. Sun, *Adv. Funct. Mater.* 20 (2010) 4175–4181.

[38] Y.H. Ding, P. Zhang, Q. Zhuo, H.M. Ren, Z.M. Yang, Y. Jiang, *Nanotechnology* 22 (2011) 215601–215605.

[39] G.L. Huang, Y.F. Zhu, *J. Phys. Chem. C* 111 (2007) 11952–11958.

[40] Q.H. Liang, W.J. Ma, Y. Shi, Z. Li, X.M. Yang, *CrystEngComm* 14 (2012) 2966–2973.

[41] J. Petroski, M.A. El-Sayed, *J. Phys. Chem. A* 107 (2003) 8371–8375.

[42] Y.M. Moustafa, K. El-Egili, *J. Non-Cryst. Solids* 240 (1998) 144–153.

[43] Y.H. Zhang, N. Zhang, Z.R. Tang, Y.J. Xu, *Phys. Chem. Chem. Phys.* 14 (2012) 9167–9175.

[44] Q. Li, B.D. Guo, J.G. Yu, J.R. Ran, B.H. Zhang, H.J. Yan, J.R. Gong, *J. Am. Chem. Soc.* 133 (2011) 10878–10884.

[45] Z.H. Chen, W.L. Wang, Z.G. Zhang, X.M. Fang, *J. Phys. Chem. C* 117 (2013) 19346–19352.

[46] D. Li, M.B. Muller, S. Gilje, R.B. Kaner, G.G. Wallace, *Nat. Nanotechnol.* 3 (2008) 101–105.

[47] P.K. Jain, X. Huang, I.H. El-Sayed, M.A. El-Sayed, *Acc. Chem. Res.* 41 (2008) 1578–1586.

[48] J. Zeng, H. Wang, Y.C. Zhang, M.K. Zhu, H. Yang, *J. Phys. Chem. C* 111 (2007) 11879–11887.

[49] Y. Kim, D. Min, *Nanoscale* 5 (2013) 3638–3642.

[50] H. Zhang, X.J. Lv, Y.M. Li, Y. Wang, J.H. Li, *ACS Nano* 4 (2010) 380–386.

[51] Y. Hou, F. Zuo, Q. Ma, C. Wang, L. Bartels, P.Y. Feng, *J. Phys. Chem. C* 116 (2012) 20132–20139.

[52] Y. Hou, X.Y. Li, Q.D. Zhao, G.H. Chen, C.L. Raston, *Environ. Sci. Technol.* 46 (2012) 4042–4050.

[53] H. Zhang, X.F. Fan, X. Quan, S. Chen, H.T. Yu, *Environ. Sci. Technol.* 45 (2011) 5731–5736.

[54] P.H. Wang, Y.X. Tang, Z.L. Dong, Z. Chen, T. Lim, *J. Mater. Chem. A* 1 (2013) 4718–4727.

[55] X. Chen, Z.F. Zheng, X.B. Ke, E. Jaatinen, T.F. Xie, D.J. Wang, C. Guo, J. Zhao, H. Zhu, *Green Chem.* 12 (2010) 414–419.

[56] J.G. Yu, G.P. Dai, B.B. Huang, *J. Phys. Chem. C* 113 (2009) 16394–16401.

[57] M. Rycenga, C.M. Cobley, J. Zeng, W. Li, C.H. Moran, Q. Zhang, D. Qin, Y.N. Xia, *Chem. Rev.* 111 (2011) 3669–3712.

[58] Q.J. Xiang, J.G. Yu, M. Jaroniec, *Chem. Soc. Rev.* 41 (2012) 782–796.